Development of Calvarial-Derived Osteogenic Cells on GDF-5 Coated Nanoporous Titanium Surfaces

metals

MDPI

Article

Development of Calvarial-Derived Osteogenic Cells on GDF-5 Coated Nanoporous Titanium Surfaces

Renan B. L. Bueno [1], Lucas N. Teixeira [1,†], Felippe J. Pavinatto [2], William M. A. Maximiano [1], Leonardo R. Zuardi [1], Adalberto L. Rosa [1], Osvaldo N. Oliveira, Jr. [2], Silvia Spriano [3] and Paulo Tambasco de Oliveira [1,*]

[1] Cell Culture Laboratory, School of Dentistry of Ribeirão Preto, University of São Paulo, Av. do Café, s/n, Ribeirão Preto 14040-904, SP, Brazil; renanbueno@gmail.com (R.B.L.B.); novaesrp@yahoo.com.br (L.N.T.); wilmaximiano@yahoo.com.br (W.M.A.M.); adalrosa@forp.usp.br (A.L.R.)
[2] São Carlos Institute of Physics, University of São Paulo, Av. Trabalhador São-Carlense, 400, São Carlos 13566-590, SP, Brazil; chu@ifsc.usp.br (O.N.O.J.)
[3] DISAT Department, Politecnico di Torino, Corso Duca degli Abruzzi 24, 10129 Torino, Italy; silvia.spriano@polito.it
* Correspondence: tambasco@usp.br; Tel.: +55-16-99623-3663
† Current address: Faculdade S. Leopoldo Mandic, R. José Rocha Junqueira, 13, Campinas 13045-755, SP, Brazil.

Abstract: This study evaluated the impact of a single variation in the etching time of H_2SO_4/H_2O_2-treated titanium (Ti) surfaces on the adsorption of growth and differentiation factor-5 (GDF-5) and their effects on the acquisition of the osteogenic phenotype in vitro. Rat primary calvarial osteogenic cells were grown for up to 14 days on the following Ti surfaces: (1) 30 min: nanotopography obtained with a 1:1 mixture of H_2SO_4/H_2O_2 for 30 min (control); (2) 30 min + GDF-5: a 30 min-etched Ti sample adsorbed with recombinant human (rh) GDF-5; (3) 4 h: nanotopography obtained with a 1:1 mixture of H_2SO_4/H_2O_2 for 4 h (control); (4) 4 h + GDF-5: a 4 h-etched Ti sample adsorbed with rhGDF-5. The GDF-5 adsorption procedure was carried out on the day before cell plating using 200 ng/mL rhGDF-5 overnight at 4 °C. The 30 min- and 4 h-etched Ti samples exhibited a high hydrophilic network of nanopits with a tendency towards larger nanopits for the 4 h group, which corresponded to an enhanced GDF-5 adsorption. For both etching times, coating with GDF-5 resulted in less hydrophilic surfaces that supported (1) a reduction in the proportion of spread cells and an enhanced extracellular osteopontin labeling at early time points of culture, and (2) increased alkaline phosphatase activity preceding an enhanced mineralized matrix formation compared with controls, with a tendency towards higher osteogenic activity for the 4 h + GDF-5 group. In conclusion, the osteogenic potential induced by the GDF-5 coating can be tailored by subtle changes in the nanotopographic characteristics of Ti surfaces.

Keywords: titanium; nanotopography; coating; GDF-5; osteoblast

Academic Editor: Antonio Riveiro

Received: 8 January 2025
Revised: 27 January 2025
Accepted: 6 February 2025
Published: 7 February 2025

Citation: Bueno, R.B.L.; Teixeira, L.N.; Pavinatto, F.J.; Maximiano, W.M.A.; Zuardi, L.R.; Rosa, A.L.; Oliveira, O.N., Jr.; Spriano, S.; de Oliveira, P.T. Development of Calvarial-Derived Osteogenic Cells on GDF-5 Coated Nanoporous Titanium Surfaces. *Metals* **2025**, *15*, 167. https://doi.org/10.3390/met15020167

1. Introduction

An implant surface in contact with bone requires several features in order to be effective. Both for orthopedic and dental devices, the main goal is to obtain a biocompatible and osseointegrable implant. In the case of titanium (Ti), its biocompatibility has been well documented. In addition, surface features can be widely modified in terms of roughness and topography—both at the micro- and nano-scale—presence of specific functional groups and/or functionalization with biomolecules to favor osseointegration [1–8]. These features play a fundamental role in the development of bone tissue around the implant, avoiding excessive inflammation and formation of fibrous tissue [9]. Another important characteristic

is the ability of implants to prevent bacterial contamination, which could lead to peri-implantitis and eventual prosthetic failure [10,11].

Implant osseointegration is mediated by a complex series of events triggered as soon as the tissues are damaged during surgery. Cytokines are released from the damaged cells and blood coagulation triggers the foreign body reaction. A layer of water molecules and proteins covers the implant surface, and then neutrophils and monocytes/macrophages are recruited at the implant site [12]. This process is modulated by the competitive adsorption of albumin and fibrinogen on the surface [13–15]. Concerning osseointegration, it takes place under an early pro-inflammatory response when mesenchymal stem cells (MSCs) differentiate into osteoblasts and/or already committed pre-osteoblasts and differentiated osteoblasts migrate to the implant surface, leading to new bone formation; it is strictly connected to the adsorption of adhesive proteins such as fibronectin [16–18]. This allows the "contact osteogenesis" mechanism with the formation of initial extracellular matrix deposition of immature bone, subsequently replaced by lamellar bone through bone remodeling. When this does not happen, the worst scenario is the proliferation of fibroblasts with the formation of a fibrous capsule, preventing an adequate contact of the implant with the parent lamellar bone [9,19].

Despite the recognized benefits that micro- and nanotopographic Ti surfaces, per se, provide for various interfacial cellular and extracellular matrix events related to bone repair [5,7], the coating of exogenous organic molecules on their surfaces—particularly on nanotopographies—can be a relevant strategy when specific biological responses are desired [2,6]. In this context, the use of natural or recombinant growth factors (GFs) is an innovative and promising approach in order to pilot the biological response of the implant [20–22]. GFs are soluble proteins secreted by different cell types, and are able to regulate their proliferation, migration and differentiation, by binding to specific transmembrane receptors on the target cells [23]. In bone, they are recognized as the main regulators of bone cell metabolism [24–26]. Thus, the peri-implant bone repair could likely benefit from the availability of a selected exogenous GF on the implant surface and in the extracellular milieu with its desorption, especially at anatomic sites with low bone density [27]. A good candidate for this could be the growth and differentiation factor 5 (GDF-5). It belongs to the transforming growth factor β (TGF-β) superfamily and plays important roles in the processes of chondrogenesis and osteogenesis [28–31]. In bone, the expression of endogenous GDF-5 has been associated with an induction of the osteoblast differentiation and enhancement of mineralized matrix production [31,32]. Deletion of either GDF-5 or bone morphogenetic protein receptor IB (BMPRIB) in mice results in a similar phenotype, indicating that GDF-5 signaling is highly dependent on this receptor, yet it also binds to BMPRIA [33]. BMPRIB activation plays an essential role in osteoblast commitment and differentiation and in bone formation in vivo [34]. Depending on the pattern of receptor interactions, the SMAD pathway or the MAPK pathway is activated [35], ultimately resulting in the expression of bone matrix genes.

Among the diverse strategies to generate nanotopographic surfaces on Ti structures, the one that uses a 4 h chemical treatment with sulfuric acid (H_2SO_4) and hydrogen peroxide (H_2O_2) has been shown to enhance the osteogenic differentiation through mechanisms that involve (i) an increase in the focal adhesions and abundance of filopodia [36], (ii) BMP-2 [37], (iii) integrin-mediated [38] and (iv) Wnt/β-catenin [39] signaling pathways. These in vitro events potentially translate into a higher proportion of bone-to-implant contact in vivo, with clinical positive effects on the outcome of implants. The subtractive technique produces simultaneous etching and oxidation of the Ti surface in a controlled manner. Importantly, other bicomponent reagents can be used for nanotexturing various implantable metals—

including Ti and its alloys—generating diverse nanogeometries that potentially exert effects on protein adsorption and cells during tissue repair [40].

The versatility of this chemical treatment allowed the observation that, in grade 2 cpTi, a reduction in the etching time from 4 h to 30 min resulted in a nanoporous Ti that inhibited the formation of non-collagenous bone matrix protein tracks secreted by osteogenic cells during their initial interactions with the surface [41]. Given that both etching protocols create similar nanotopographies, the present study aimed to evaluate the effects of GDF-5-coated nanoporous Ti surfaces on the acquisition of the osteogenic phenotype in vitro. Our hypothesis is that subtle changes in the nanotopographic features due to the variation in the etching time might modulate the biological action of GDF-5 on bone-derived cells.

2. Materials and Methods

2.1. Preparation of Nanotopographic Ti Surfaces and Coating with GDF-5

Commercially pure, grade 2 Ti discs, 13 mm in diameter and 2 mm thick (Realum, São Paulo, Brazil), were polished with silicon carbide abrasive papers (320 and 600 grit), cleaned by sonication, rinsed with toluene, and treated with a mixture consisting of equal volumes of concentrated H_2SO_4 (95–97%) and 30% H_2O_2 (10 mL/disc) for 30 min or 4 h (control surfaces) at room temperature (RT) under continuous agitation [41,42]. The cleaned, oxidized samples were thoroughly rinsed with distilled water, autoclaved and air-dried. On the day before the cell culture experiments, the nanoporous Ti discs were incubated overnight at 4 °C with 200 ng/mL GDF-5 (recombinant human GDF-5, Peprotech, Mexico City, Mexico) in 24-well polystyrene plates, and then washed three times with phosphate buffered saline (PBS) at 37 °C. The experimental groups were then defined as follows: (i) 30 min: Ti surfaces etched with a mixture of H_2SO_4/H_2O_2 for 30 min (control); (ii) 30 min + GDF-5: Ti surfaces etched with a mixture of H_2SO_4/H_2O_2 for 30 min and coated with GDF-5; (iii) 4 h: Ti surfaces etched with a mixture of H_2SO_4/H_2O_2 for 4 h (control); (iv) 4 h + GDF-5: Ti surfaces etched with a mixture of H_2SO_4/H_2O_2 for 4 h and coated with GDF-5.

2.2. Surface Characterization

2.2.1. Surface Chemistry of Control Non-Coated Ti

The surface chemistry of the etched Ti surfaces was analyzed by XPS measurements (XPS, PHI 5000 Versaprobe II, ULVAC-PHI Inc., Kanagawa, Japan); a non-etched surface was used as control. The X-rays were generated by an Al–K source and the take-off angle was 45°. Survey spectra were recorded to determine the elemental composition, while high-resolution spectra of the C1s and O1s regions were acquired with a pass energy of 0.1 eV. Before the deconvolution, the spectra were calibrated by setting the C1s peak (the C–C bond) at 284.8 ± 0.1 eV.

2.2.2. Surface Topography and Wettability of GDF-5-Coated Nanotopographies

The surface of randomly selected treated Ti discs was qualitatively and quantitatively evaluated in terms of topography and wettability. Scanning electron microscopy (SEM) imaging was carried out using a JEOL JSM-7400F field emission scanning electron microscope (JEOL Ltd., Tokyo, Japan) operated at 1.5 kV. The nanopit diameters (n = 100 for each surface) were measured using the ImageJ software Version 1.54g (NIH, Bethesda, MD, USA). In addition, surface topography was visualized by atomic force microscopy (AFM) in the tapping mode, employing a resonance frequency of approximately 300 kHz, scan rate of 1.0 Hz, and scanned areas of 10 × 10 µm, 5 × 5 µm and 1 × 1 µm, using a Nanoscope IIIa atomic force microscope (Digital Instruments, Santa Barbara, CA, USA). The tip was made from silicon. The recorded topographic images were analyzed with WinSPM Data

Processing Software (version 2.15, JEOL Ltd.) in order to determine root mean square roughness (RMS) values. Regarding surface wettability, the immediate (time 0) and equilibrium (at 5 min) static contact angles were measured using the sessile drop method [43] with a video-based contact angle meter, using a drop of the supplemented cell culture medium (see composition described in Section 2.3.1), which contained 10% fetal bovine serum (FBS), onto Ti surfaces (n = 3) at 28.7 °C (CAM200, KSV Instruments, Helsinki, Finland).

2.2.3. Polarization-Modulated Infrared Reflection Absorption Spectroscopy (PM-IRRAS) of GDF-5-Functionalized Nanotopographies

PM-IRRAS was performed using a KSV PMI 550 instrument (KSV Instruments). The Langmuir trough is positioned with the light beam reaching the monolayer at a fixed incidence angle of ~80°, at which the intensity is maximum with a reduced noise level. Downward bands in the spectrum indicate transition moments oriented preferentially perpendicular to the surface, whereas upward absorption bands are assigned to transition moments oriented preferentially parallel to the surface plane. The incoming light is continuously modulated between s-polarization and p-polarization at a high frequency (50 kHz), which allows simultaneous measurement of the spectra for the two polarizations. The difference thus provides surface-specific information, and the sum represents the reference spectrum. Since the spectra are measured simultaneously, the effect of water vapor is reduced. Measurements were performed at 20 °C and with SEPT2 (70 nM) heated at 37 °C for 30 min prior to the experiment. Ti discs were spread at 5 mN/m and then SEPT2 was added to the subphase. The compression was performed every 5 mN/m up to a surface pressure of 40 mN/m.

2.3. Biological Experiments

2.3.1. Cell Isolation and Primary Culture of Osteogenic Cells

Primary osteogenic cells were isolated by sequential trypsin/collagenase digestion of calvarial bone from newborn (2–4 days) Wistar rats [42]. All animal procedures were in accordance with guidelines of the Animal Research Ethics Committee of the University of São Paulo (protocol #08.1.836.53.1). Primary cells were plated on GDF-5-coated 30 min- and 4 h-etched Ti discs and their controls placed in 24-well polystyrene plates (Falcon, Franklin Lakes, NJ, USA) at a cell density of 2×10^4 cells per disc. Neither subcultured cells nor passaged cells were used for the experiments. The plated cells were then grown for periods up to 14 days in Gibco α-Minimum Essential Medium with L-glutamine (Invitrogen, Carlsbad, CA, USA) supplemented with 10% FBS (Invitrogen), 7 mM β-glycerophosphate (Sigma, St. Louis, MO, USA), 5 µg/mL ascorbic acid (Sigma), and 50 µg/mL gentamicin (Invitrogen) at 37 °C in a humidified atmosphere with 5% CO_2. The culture medium was changed every 3 days. The progression of cultures was examined by phase contrast microscopy of cells grown on polystyrene.

2.3.2. Cell Adhesion and Spreading

Cell adhesion and spreading were evaluated by direct fluorescence with Alexa Fluor 488-conjugated phalloidin (Molecular Probes, Eugene, OR, USA), which labels ubiquitous actin cytoskeleton, and 4′,6-diamidino-2-phenylindole, dihydrochloride (DAPI, Molecular Probes), for nuclear stain (see details in Section 2.3.4). To assess the stage of adhesion and spreading [44], the proportion of cells at stage 1 (round cells), 2 (round cells with filopodia), 3 (cells with cytoplasmic webbing), and 4 (well flattened cells) was calculated out of 100 adherent cells at 4 h for each surface, using randomly selected microscopic fields (x40 objective).

2.3.3. Cell Viability

Cell viability was evaluated by 3-[4,5-dimethylthiazol-2-yl]-2,5-diphenyltetrazolium bromide (MTT, Sigma) assay at days 1, 3, and 7 of culture [45]. Firstly, the Ti discs containing the primary cultures were moved to new 24-well polystyrene plates (Falcon), and cells were incubated with 1 mL of MTT (5 mg/mL) in culture medium at 37 °C for 4 h. The medium was then aspirated from the well, and 1 mL of acid isopropanol (0.04 N HCl in isopropanol) was added to each well. The plates were then stirred on a plate shaker for 5 min, and 200 µL of this solution was transferred to a 96-well format using opaque-walled transparent-bottomed plates (Fisher Scientific, Suwanee, GA, USA). The optical density was read at 570 nm on the plate reader (µQuanti, BioTek Instruments, Winooski, VT, USA), and data were expressed as absorbance.

2.3.4. Epifluorescence for Cell Morphology and Osteopontin Immunolocalization

At day 3 of culture, cells were fixed for 10 min at RT using 4% paraformaldehyde in 0.1 M sodium phosphate buffer (PB), pH 7.2. After washing in PB, the cultures were processed for fluorescence labeling [42]. Briefly, the cells were permeabilized with 0.5% Triton X-100 in PB for 10 min and were then blocked with 5% skim milk in PB for 30 min. Primary monoclonal antibody against osteopontin (1:800, MPIIIB10-1, Developmental Studies Hybridoma Bank, Iowa City, IA, USA) was used, followed by Alexa Fluor 594-conjugated goat anti-mouse secondary antibody (1:200, Molecular Probes) and Alexa Fluor 488-conjugated phalloidin (1:200, Molecular Probes). All incubations were performed in a humidified environment for 60 min at RT. Between each incubation step, the cells were washed in PB (3 × 5 min). Before mounting for microscope observation, the cells were briefly washed with distilled water, and the cell nuclei were stained with 300 nM DAPI (Molecular Probes) for 5 min. A glass coverslip was mounted with an antifade kit (Vectashield, Vector Laboratories, Burlingame, CA, USA) on the nanotopographic Ti surfaces containing the cells. The samples were then examined under epifluorescence using a Leica DMLB microscope (Leica Microsystems, Wetzlar, Germany) outfitted with a Leica DC 300F digital camera (Leica Microsystems), and the acquired images were processed using Adobe Photoshop CS5.1 software, version 12.1 x64 (Adobe Systems, San Jose, CA, USA).

2.3.5. Real-Time Polymerase Chain Reaction (Real-Time PCR) for Osteoblast Markers

Gene expression of runt-related transcription factor 2 (Runx2), alkaline phosphatase, bone sialoprotein, and osteopontin was evaluated by Real-time PCR at days 7 and 10 of culture. The total RNA from cells was extracted using the SV Total RNA Isolation System Kit (Promega, Madison, WI, USA), according to the manufacturer instructions. The concentration of RNA was determined by optical density at different wavelengths (260, 280, 230 e 320 nm) using the GeneQuant 1300 spectrophotometer (GE Healthcare, Cardiff, UK). Complementary DNA (cDNA) was synthesized using 1 µg of RNA through a reverse transcription reaction using High Capacity cDNA Reverse Transcription Kit (Applied Biosystems, Foster City, CA, USA), according to the manufacturer instructions. Real-time PCR was performed in a CFX96 (Bio-Rad Laboratories, Hercules, CA, USA) using TaqMan® (Applied Biosystems). The reactions of Real-time PCR performed by the TaqMan probe were prepared for a final volume of 10 µL per reaction. For each reaction were added 5 µL of TaqMan Universal PCR Master Mix-No AmpErase UNG (2X), 0.5 mL of TaqMan probes for target genes (20X TaqMan Gene Expression Assay Mix) and 11.25 ng of cDNA. The standard PCR conditions were 50 °C (2 min), 95 °C (10 min), and 40 cycles of 95 °C (15 s), 60 °C (1 min), followed by the standard denaturation curve. The results were analyzed based on the Ct value (cycle threshold) and all samples were subjected to reactions to detect messenger RNA for the constitutively expressed gene Gapdh and a negative sample (water)

was subjected to the reaction with each TaqMan probe used. Normalization and relative quantification of gene expression were performed using the $2^{-\Delta\Delta CT}$ method [46]. Data were then represented as difference (in folds) in gene expression normalized by the constitutive gene. A value of 1 was assigned to each marker for cultures on non-etched Ti at day 7 (calibrator), thus allowing comparisons among groups and between experimental times.

2.3.6. Alkaline Phosphatase Activity

Alkaline phosphatase activity was assayed at days 7 and 10 of culture by means of the release of thymolphthalein from thymolphthalein monophosphate using a commercial kit (Labtest Diagnóstica, Lagoa Santa, Brazil). Briefly, 50 µL of thymolphthalein monophosphate was mixed with 0.5 mL of 0.3 M diethanolamine buffer, pH 10.1, and left for 2 min at 37 °C. The solution was then added to 50 µL of the lysates obtained from each well for 10 min at 37 °C. For color development, 2 mL of 0.09 M Na_2CO_3 and 0.25 M NaOH were added. After 30 min, absorbance was measured at 590 nm and alkaline phosphatase activity was calculated from a standard curve using thymolphthalein to give a range from 0.012 to 0.4 µmol thymolphthalein/h/mL. Data were expressed as alkaline phosphatase activity normalized for total protein content, which was determined by modified Lowry method [47].

2.3.7. Mineralized Bone-like Nodule Formation

At day 14 of culture, the cell cultures were washed in Hanks solution, fixed in 70% ethanol at 4 °C for 60 min and washed in PBS and distilled water. The cultures were then stained with 2% Alizarin Red S (ARS), pH 4.2, at RT for 15 min. The macroscopic images were obtained digitally by a high-resolution camera (Canon EOS Digital Rebel, 6.3 megapixels, EF100 f/2.8 macro lens; Canon, Lake Success, NY, USA). Biochemically, the quantitation of mineralization was evaluated by the ARS extraction method [48]. Briefly, 280 µL of 10% acetic acid was added in each well containing the Ti samples with the ARS-stained cultures, and the plate was gently shaken for 30 min. Cultures were then scraped and the solution transferred to 1.5 mL tubes and vortexed for 30 s. The tubes were heated to 85 °C for 10 min, transferred to ice for 5 min and then centrifuged at 13,000× *g* for 20 min. In each experimental group, 100 µL of supernatant was transferred to a 96-well plate and 40 µL of 10% NH_4OH was added. The samples were read on a spectrophotometer (µQuanti, BioTek Instruments) at a wavelength of 405 nm. The standard curve was performed with successive dissolutions of ARS from 0.5 to 3 mM in ammonium acetate (10% glacial acetic acid and 5 M NH_4OH).

2.4. Statistical Analyses

Comparisons were performed using the parametric one-way or two-way ANOVA tests, followed by Tukey's test for multiple comparisons where applicable. The level of significance was set at 5%. The results are representative of experiments performed with at least three distinct primary cultures. Due to the relatively limited number of isolated primary cells derived from calvarial bone of newborn rats in each litter (~12 animals/litter), for each technique involving cells, one biological replicate/primary cell culture was used, with five experimental replicates/wells and one technical replicate per group and per time point. The software used for statistics was GraphPad Prism 5.0 (GraphPad Software, San Diego, CA, USA).

3. Results

3.1. Surface Characterization

XPS survey analysis detected C, which is an unavoidable surface contamination, Ti, and O, with a Ti/O ratio in the range of 0.3–0.4 (Figure 1A–C). The profile fitting of the oxygen region (Figure 1D–F) evidenced the presence of TiO_2 (the main peak at 529.97–530.03 eV) and hydroxyl groups both with acidic (530.84–531.06 eV) and basic (531.76–532.07 eV) reactivity. The contribution of the two types of hydroxyl groups to the total area of the O1s peak was decreasing, moving to non-etched Ti (36%), to 30 min-etched Ti (33%) and 4 h-etched Ti (32%), respectively. Secondarily, the ratio of the acidic to basic groups was about 3 in the case of non-etched Ti, while it was almost 1 for both 30 min-etched Ti and 4 h-etched Ti, with an evident increase in the basic hydroxyl groups after etching.

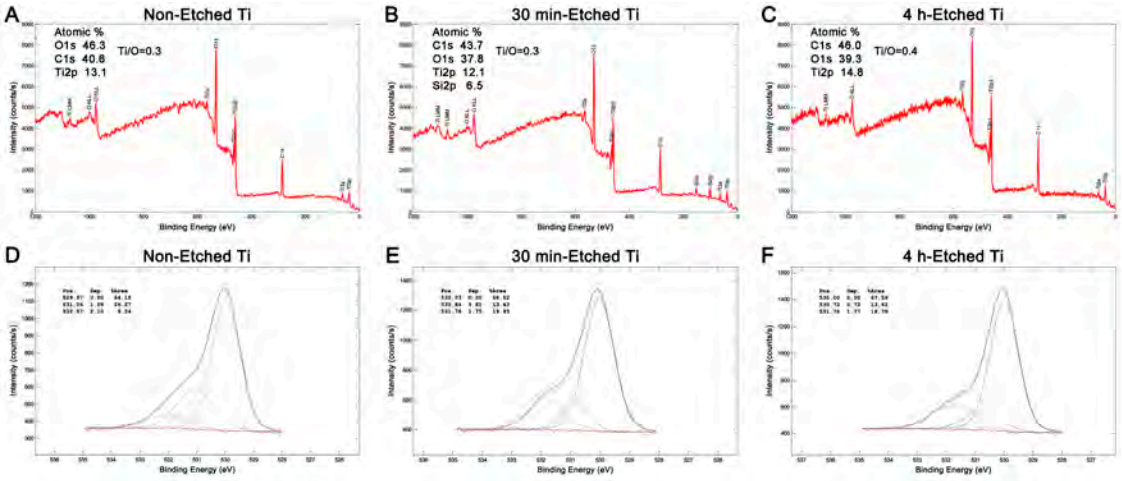

Figure 1. Survey X-ray photoelectron spectroscopy (XPS) spectra (**A**–**C**) and high-resolution XPS spectra of O1s peak (**D**–**F**). Panels show XPS of non-etched Ti (**A**,**D**), 30 min- (**B**,**E**) and 4 h-etched Ti (**C**,**F**).

High-resolution SEM analysis revealed that the protocols used to chemically treat Ti surfaces result in the formation of a network of nanopits (Figure 2), with a tendency towards larger pits for the 4 h groups (in Figure 2, compare C and D with A and B); the mean nanopit diameter for the 30 min group was 15.7 nm (± 3.6 nm), and for the 4 h group, it was 21.7 nm (±6.7 nm). No impact on the topographic features at the nanoscale was noted with the adsorption of GDF-5 (in Figure 2, compare B with A, and D with C). The results of AFM revealed that RMS is in the order of 6 nm for 30 min-etched Ti and ~8 nm for the 4 h group, and that the GDF-5 coating reduces RMS in the order of 1 nm for both groups (Figure S1).

The PM-IRRAS analysis revealed bands at 1650, 1551 and 1402 cm^{-1} for either 30 min + GDF-5 or 4 h + GDF-5 groups, with enhanced signals for the latter (Figure 3; compare the blue and the green lines). Variations in the PM-IRRAS intensity were detected depending on the region of the Ti surface evaluated (Figure S2; compare the red and the blue lines). No bands were present in the spectrum for either 30 min-etched or 4 h-etched Ti surfaces (Figure 3, black and red lines).

Using a drop of the cell culture medium, all the surfaces were well wetted with contact angles lower than 90°. The Ti surfaces coated with GDF-5 presented greater mean values of static contact angles initially and at equilibrium compared with the non-coated surfaces, except for 4 h + GDF-5 at equilibrium, with only a tendency towards higher values

(Figure 4). In addition, for the GDF-5-coated surfaces, the contact angles at equilibrium were significantly reduced compared with the initial ones.

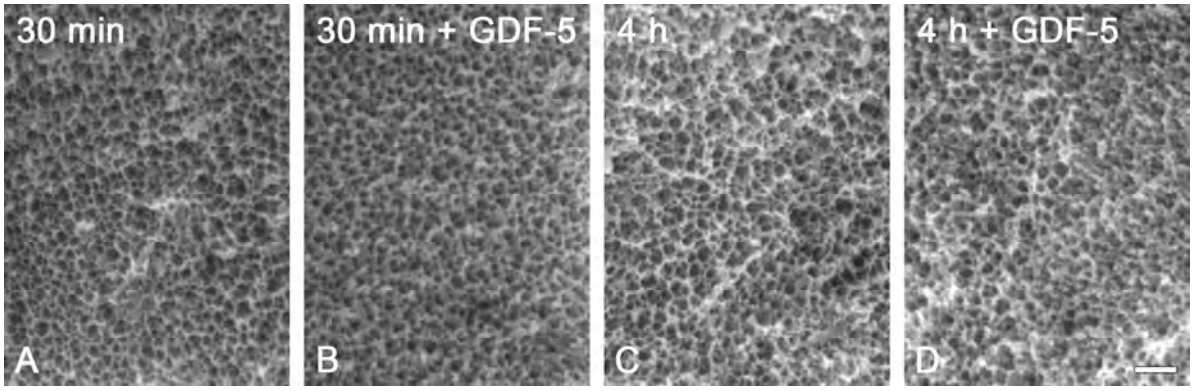

Figure 2. High-resolution SEM imaging of 30 min, 30 min + GDF-5, 4 h and 4 h + GDF-5 etched Ti surfaces (**A**–**D**). Relatively larger nanopits were observed in Ti surfaces etched for 4 h compared with the ones etched for 30 min. The adsorption of GDF-5 had no impact on the topographic features at the nanoscale. Scale bar = 100 nm (**A**–**D**).

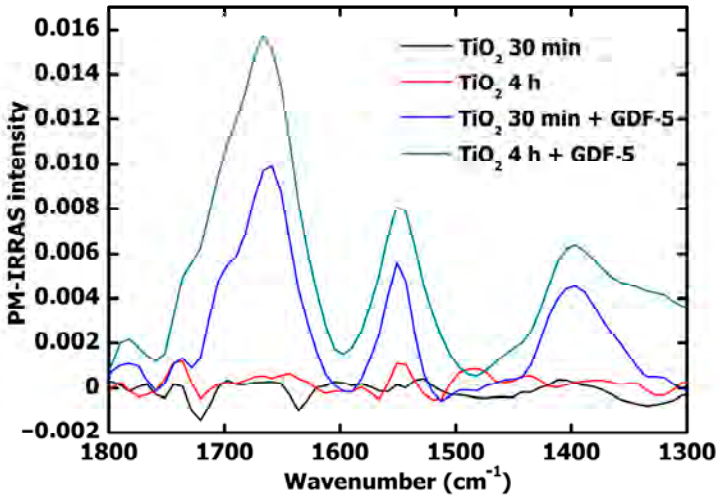

Figure 3. Polarization modulation infrared reflection adsorption spectroscopy (PM-IRRAS) of the chemically treated, GDF-5-coated Ti surfaces. Adsorption of GDF-5 was detected in the coated Ti surfaces, with a greater signal for the 4 h + GDF-5 surface (green line). No significant signals were detected for either 30 min-etched or 4 h-etched surfaces (controls, black and red lines, respectively).

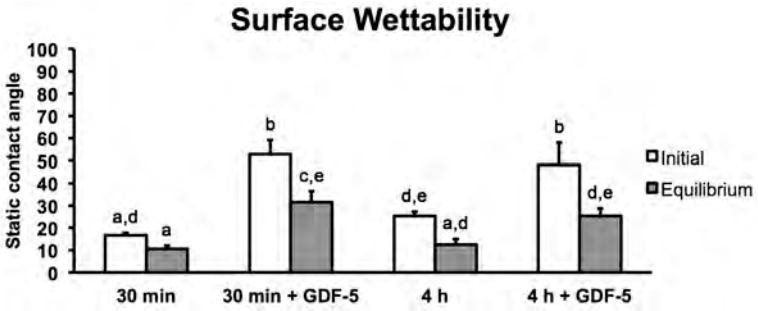

Figure 4. Surface wettability analysis by means of the sessile drop method, using a drop of the cell culture medium. The static contact angles for the GDF-5-coated surfaces were significantly higher compared with the control etched ones both initially and at equilibrium, except for 4 h + GDF-5 at equilibrium (only a tendency towards higher values). For the GDF-5-coated surfaces, the contact angles at equilibrium were significantly reduced compared with the initial ones. Bars that share at least one letter are not significantly ($p > 0.05$) different from each other.

3.2. Biological Experiments

Cell adhesion and spreading analysis at 4 h of culture revealed a significant decrease in the proportion of cells at stages 3 and 4 of spreading for the GDF-5-coated surfaces compared with the corresponding non-coated ones (Figure 5 and Figure S3).

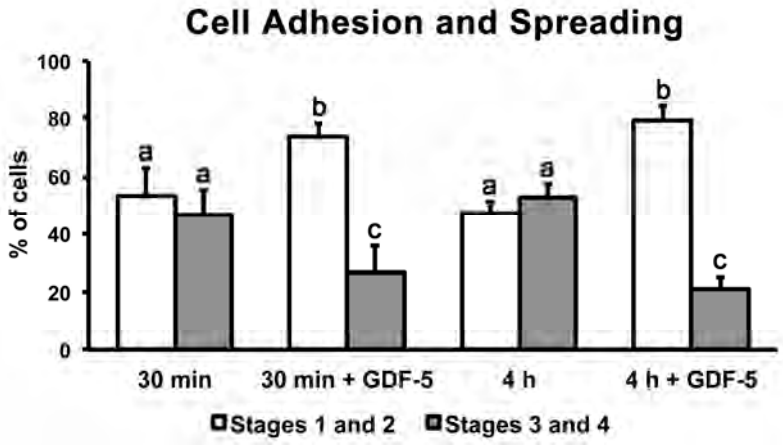

Figure 5. Proportion of primary osteogenic cells at different stages of adhesion and spreading at 4 h of culture. The nanoporous Ti surfaces coated with GDF-5 presented a significantly reduced proportion of cells at more advanced stages of spreading. Bars that share at least one letter are not significantly ($p > 0.05$) different from each other.

The MTT assay results showed no significant differences among groups within a given time point—1, 3, or 7 days of culture—with the highest values for cells grown on all surfaces at day 7 of culture (Figure 6).

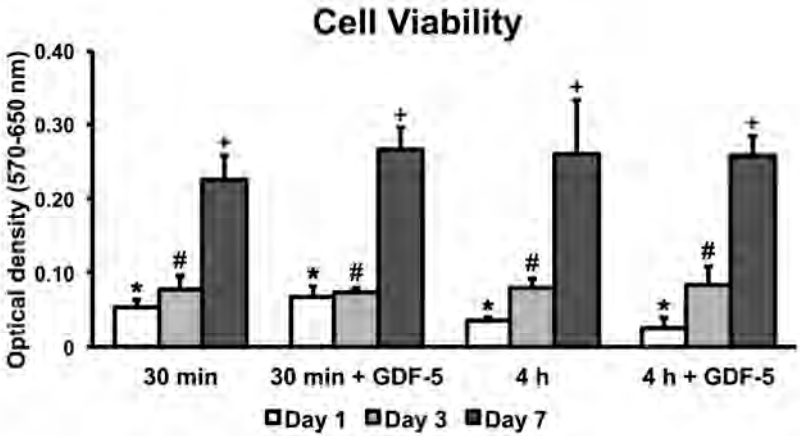

Figure 6. Cell viability (MTT, optical density) of primary osteogenic cell cultures grown on 30 min, 30 min + GDF-5, 4 h and 4 h + GDF-5 etched surfaces at days 1, 3, and 7 of culture. Within a given time point, there were no significant differences among groups. Bars that share one symbol (*, #, or +) are not significantly ($p > 0.05$) different from each other.

At day 3 of culture, epifluorescence analysis revealed a perinuclear pattern of osteopontin labeling in the majority of cells grown on all surfaces. However, extracellular osteopontin accumulation was noted only for the 30 min + GDF-5, 4 h and 4 h + GDF-5 etched surfaces, which was clearly most abundant for the GDF-5-coated surfaces (Figure 7).

The real-time PCR analysis (Figure 8) showed that the Runx2 and alkaline phosphatase mRNA levels significantly decreased from day 7 to 10 of culture for all surfaces, with differences between coated and non-coated surfaces only for 4 h + GDF-5 at day 10 of culture, which exhibited the lowest Runx2 and alkaline phosphatase mRNA levels (Figure 8A,B).

The bone sialoprotein mRNA levels significantly decreased from day 7 to 10 of culture for all surfaces except for the 30 min-etched one, which showed no differences between these two time points. Differences between coated and non-coated surfaces were observed for 4 h + GDF-5 at day 7 of culture, exhibiting the highest bone sialoprotein mRNA levels, and for 30 min + GDF-5 and 4 h + GDF-5 at day 10 of culture, with the lowest levels (Figure 8C). The osteopontin mRNA levels significantly increased from day 7 to 10 of culture for all surfaces except for the 30 min + GDF-5, which showed no differences between these two time points. Whereas, at day 7 of culture, no differences in the osteopontin mRNA levels were observed between coated and non-coated surfaces, at day 10 of culture, a significant reduction in its levels was observed for the coated surfaces (Figure 8D).

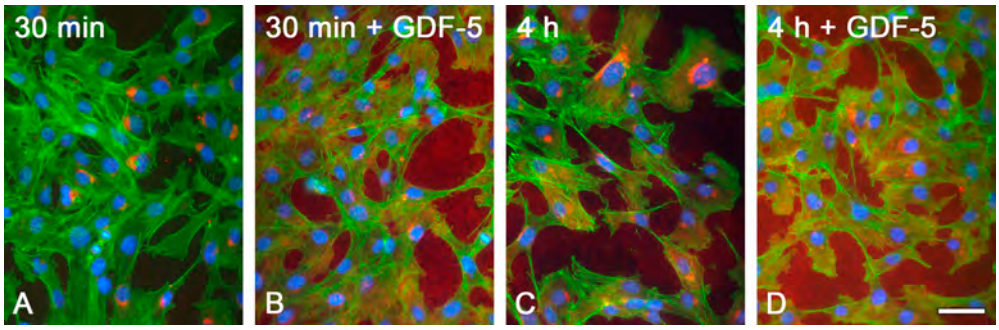

Figure 7. Epifluorescence of primary osteogenic cell cultures grown on 30 min, 30 min + GDF-5, 4 h and 4 h + GDF-5 etched surfaces at day 3 of culture (**A**–**D**). Extracellular osteopontin labeling (red fluorescence) was abundant and more prominent in cultures grown on GDF-5-coated Ti surfaces (compare (**B**) and (**D**) with (**A**) and (**C**), respectively); perinuclear Golgi labeling (red fluorescence) was clearly visible (**A**–**D**). The green fluorescence indicates the F-actin cytoskeleton (Alexa Fluor 488-conjugated phalloidin), whereas the blue fluorescence depicts cell nuclei (DAPI DNA stain). Scale bar = 50 μm (**A**–**D**).

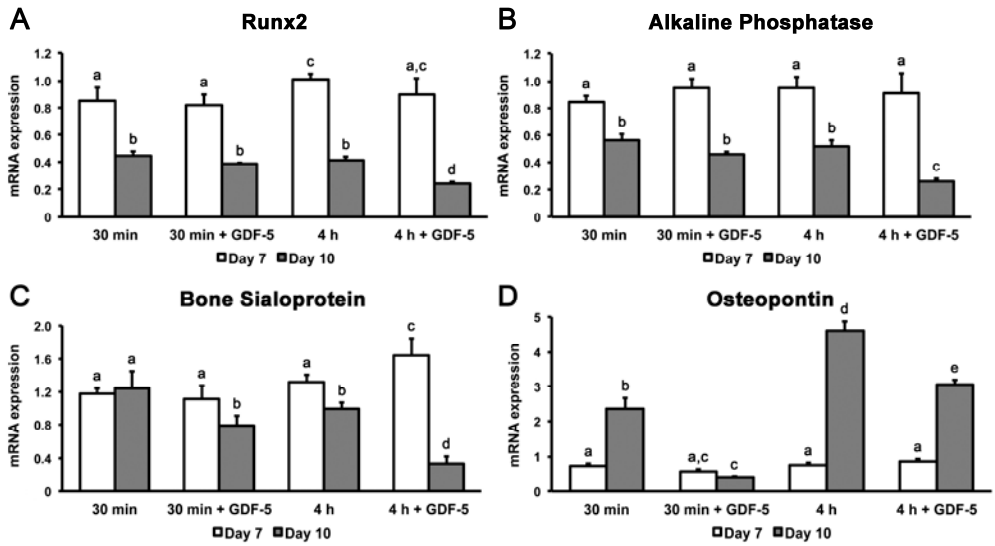

Figure 8. Real-time polymerase chain reaction (PCR) analysis of Runx2 (**A**), alkaline phosphatase (**B**), bone sialoprotein (**C**), and osteopontin (**D**) mRNA expression in primary osteogenic cell cultures grown on 30 min, 30 min + GDF-5, 4 h and 4 h + GDF-5 etched surfaces at days 7 and 10 of culture. Data were normalized for Gapdh mRNA levels and calibrated to value 1 with cultures on non-etched surface at day 7. Bars that share at least one letter are not significantly ($p > 0.05$) different from each other.

The alkaline phosphatase activity significantly increased from day 7 to 10 of culture on all surfaces. Whereas, at day 7, no significant differences were observed among surfaces, at

day 10, the 4 h + GDF-5 surface exhibited significantly higher alkaline phosphatase activity compared with the 4 h-etched group (Figure 9).

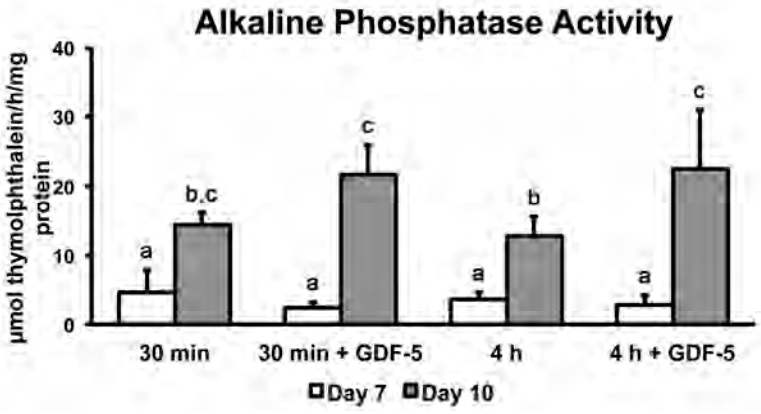

Figure 9. Alkaline phosphatase activity (µmol thymolphthalein/h/mg protein) of primary osteogenic cell cultures grown on 30 min, 30 min + GDF-5, 4 h and 4 h + GDF-5 etched Ti surfaces at days 7 and 10 of culture. A significant increase in alkaline phosphatase activity was observed from day 7 to 10 of culture, with peak levels for the GDF-5-coated surfaces at day 10. Bars that share at least one letter are not significantly ($p > 0.05$) different from each other.

At day 14 of culture, typical mineralized nodule formations, reddish/brownish in color and surrounded by diffuse ARS-stained areas with variable extensions, were noted on all surfaces (Figure 10A). Significantly higher values of ARS extraction were detected in cultures grown on GDF-5-coated Ti surfaces (Figure 10B).

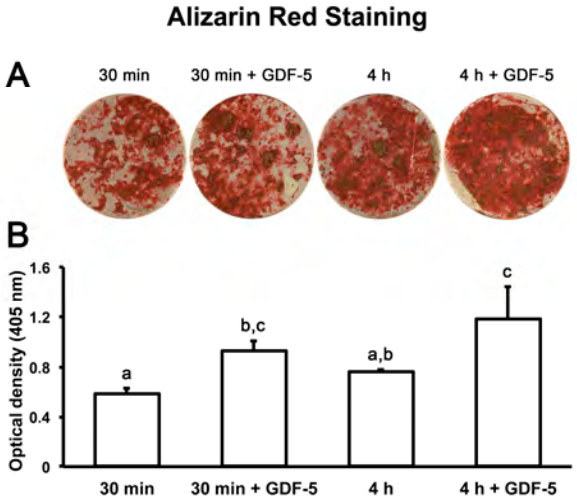

Figure 10. (**A**) Macroscopic imaging of primary osteogenic cell cultures grown on 30 min, 30 min + GDF-5, 4 h and 4 h + GDF-5 etched Ti surfaces at day 14 of culture, and stained with Alizarin red S (ARS) for detecting calcium deposits. Nodular and diffuse patterns of mineralization were observed on all surfaces. (**B**) Quantitative analysis of the ARS-stained primary osteogenic cell cultures shows significantly higher mineralization for the GDF-5-coated surfaces. Bars that share at least one letter are not significantly ($p > 0.05$) different from each other.

4. Discussion

The results of this in vitro study demonstrated that a single variation in the etching time of H_2SO_4/H_2O_2-treated Ti surfaces affects the amounts of adsorbed GDF-5. Both the 30 min- and 4 h-etched surfaces exhibited a characteristic network of nanopits with a tendency towards larger nanopits for the 4 h-etched one, which corresponded to a trend towards enhanced GDF-5 adsorption, as detected by PM-IRRAS. All the sur-

faces (before and after GDF-5 coating) turned out to be well wetted by the cell culture medium. The high wettability by the cell culture medium, containing proteins, can explain the positive biological behavior of these surfaces [42]. In addition, irrespective of the etching time, the coating with GDF-5 resulted in surfaces less wetted by the cell culture medium at equilibrium than the ones before coating (30 min-etched and 4 h-etched control Ti)—even if maintaining a good wettability—and affected key parameters of the acquisition of the osteogenic phenotype by rat primary calvarial cells, showing (1) a reduction in the proportion of spread cells and an enhanced extracellular osteopontin labeling at early time points of culture, and (2) increased alkaline phosphatase activity, which preceded an enhanced mineralized matrix formation compared with controls. A tendency towards higher osteogenic activity for the 4 h + GDF-5 surface at day 14 of culture corresponded with higher bone sialoprotein mRNA levels at the onset of osteoblastic differentiation (day 7 of culture).

The coating of metals with bioactive molecules, aiming to promote interfacial bone tissue formation during the healing process, has been a challenge. Indeed, several surface coatings with organic molecules that are endogenously expressed during interfacial tissue healing have been used, with controversial and unpredictable outcomes [49–51]. In the present study, we opted to use the simple, yet versatile, strategy to chemically etch Ti with a mixture of H_2SO_4/H_2O_2 and to coat the resulting nanoporous surfaces with GDF-5, a growth factor with known stimulatory effects on bone formation [31,32]. In addition to the 4 h etching protocol, which has been shown to modulate signaling pathways in osteoblastic cells and to support the osteogenic phenotype in vitro [36–39] and in vivo [52], a shorter etching time was also chosen to evaluate the impact of fine-tuning nanotopography on the GDF-5 coating, with the benefit of accelerating the surface preparation protocol. Importantly, strategies to shorten the acidic functionalization of metallic implants would limit detrimental effects, if any, on their surface structure and mechanical resistance [53].

Although the qualitative numerical data indicated that the 30 min etching supported a trend towards lower amounts of adsorbed GDF-5, associated with a tendency towards smaller nanopores and reduced values of nanoroughness, the presence of GDF-5 also promoted the in vitro osteogenic events on this surface, comparable to the ones on the 4 h-etched surface. The secondary structure of GDF-5 was likely similar for both groups, as indicated by the amide I (1700–1600 cm^{-1}) and the amide II (1600–1500 cm^{-1}) spectra regions, suggesting a high bioactivity of GDF-5 when coated on both nanotopographies [54]. Considering that the desorption of GDF-5 is expected during the first days of culture, as dip coating supports burst release [55], the amount of GDF-5 in the extracellular milieu would likely be similar for both 30 min and 4 h groups, i.e., within the same range of stimulatory concentrations, thus resulting in similar tissue phenotypic characteristics at day 14 of culture. Interestingly, the trend of a transient reduction of about 50% in the MTT values in the 4 h + GDF-5 group could be due to an initial higher release of GDF-5 from the nanoporous surface; as the culture progressed to days 3 and 7, this effect was no longer observed. Despite the osteogenic stimulatory effects obtained with 200 ng/mL of GDF-5 coating solution in the present study, with benefits of avoiding potential side effects, as observed for some BMP therapies [56], any translational GDF-5 application might consider higher doses in the microgram range [57,58].

Prior to the cell culture experiments, the presence of adsorbed GDF-5 was also indirectly detected by the changes in surface wettability it induced. It has been well established that the chemical etching of Ti with the H_2SO_4/H_2O_2 mixture generates a highly hydrophilic TiO_2 nanotopography [42]. The results of the sessile drop method showed that the GDF-5 coating enhanced the contact angle of a drop of supplemented cell culture medium at equilibrium, thus resulting in a less wetted surface. This finding is supported

by the chemical nature of GDF-5, which as a GF that belongs to the TGF-β superfamily, contain a hydrophobic N-terminal signal sequence [59]. Interestingly, the tendency to hydrophobicity led to reduced cell spreading at 4 h of culture and increased extracellular osteopontin accumulation at day 3 of culture, which are cellular events that have been associated with an earlier acquisition of the mature osteoblastic phenotype [42,60].

While the surface characterization unequivocally revealed an inhomogeneous GDF-5 coating on nanoporous Ti, its biological functionality could be confirmed by an increased alkaline phosphatase activity, which was associated with an enhancement in the extracellular matrix mineralization [61–63]. Despite the complexity of the data generated by the quantitative mRNA analysis of osteoblast markers, which reveals that there may be no correlation between the expression of an mRNA and the protein it encodes [64,65], the phenotypic changes in cultures exposed to GDF-5 could be explained, at least in part, by the results of osteopontin expression. The observed downregulation of osteopontin during the mineralization phase of cultures likely reduced its inhibitory effect on mineral deposition [66,67] and/or was associated with a more advanced stage of the osteogenic process [68]. Additionally, an upregulation of bone sialoprotein—a nucleator of apatite crystals [69–71]—at the onset of osteoblastic differentiation preceded the highest osteogenic potential of cultures grown on the 4 h-etched, GDF-5-coated Ti, rendering bone sialoprotein a possible earlier marker of bone-like nodule formation in the in vitro model used.

5. Conclusions

In conclusion, the strategy to coat GDF-5 on chemically produced nanotopographies obtained by two distinct H_2SO_4/H_2O_2 etching times ensures its biological activity, which supports an enhancement in the osteogenic potential in vitro. Despite some differences between 30 min- and 4 h-etched Ti in terms of physico-chemical surface properties and parameters related to the acquisition of the osteogenic phenotype, the similarities in the outcomes of cell cultures, i.e., amounts of mineralized matrix formation, lead us to consider the shorter etching time as a useful tool in strategies to functionalize growth factors and potentially other bioactive molecules aiming to promote specific cell and tissue responses at the biomaterial–bone interface.

Supplementary Materials: The following supporting information can be downloaded at: https://www.mdpi.com/article/10.3390/met15020167/s1, Figure S1: Atomic force microscopy (AFM) topographies (1×1 μm^2) (A) and surface nanoroughness (RMS) (B) of 30 min, 30 min + GDF-5, 4 h and 4 h + GDF-5 etched titanium surfaces. Figure S2: Polarization modulation infrared reflection adsorption spectroscopy (PM-IRRAS) of the 30 min-etched titanium surface coated with GDF-5. Variations in the PM-IRRAS intensity were detected depending on the region of the surface evaluated (compare the red and the blue lines). Figure S3: Epifluorescence of primary osteogenic cell cultures grown on 30 min, 30 min + GDF-5, 4 h and 4 h + GDF-5 etched surfaces at 4 h of culture (A–D). The green fluorescence indicates the F-actin cytoskeleton (Alexa Fluor 488-conjugated phalloidin), whereas the blue fluorescence reveals cell nuclei (DAPI DNA stain). In A, the stages of cell adhesion and spreading, according to Rajaraman et al. (1974), are indicated as follows: 1, a round cell; 2, a round cell with filopodia; 3, a cell with cytoplasmic webbing; 4, a well flattened cell. Scale bar = 50 μm (×40 objective for A–D).

Author Contributions: Conceptualization, P.T.d.O.; methodology, R.B.L.B., L.N.T., F.J.P., L.R.Z., A.L.R., O.N.O.J., S.S. and P.T.d.O.; formal analysis/investigation, R.B.L.B., L.N.T., F.J.P., W.M.A.M., L.R.Z., A.L.R., O.N.O.J., S.S. and P.T.d.O.; writing—original draft preparation, R.B.L.B., L.N.T., W.M.A.M. and P.T.d.O.; writing—review and editing, R.B.L.B., L.N.T., W.M.A.M., S.S. and P.T.d.O.; visualization, R.B.L.B., L.N.T., F.J.P., W.M.A.M., L.R.Z., A.L.R., O.N.O.J., S.S. and P.T.d.O.; supervision, P.T.d.O.; project administration, P.T.d.O.; funding acquisition, P.T.d.O. All authors have read and agreed to the published version of the manuscript.

Funding: This research was funded by the National Council for Scientific and Technological Development (CNPq)—Brazil, grant number 315266/2020-1 (scholarship on research productivity to P.T.O.), and the State of São Paulo Research Foundation (FAPESP)—Brazil (grant 18/22214-6 to O.N.O.J.; scholarships 08/55575-0 and 11/50342-0 to R.B.L.B., and 12/08605-6 to L.N.T.).

Data Availability Statement: The original contributions presented in this study are included in the article/Supplementary Materials. Further inquiries can be directed to the corresponding author.

Acknowledgments: The authors thank Antonio Nanci, from the Laboratory for the Study of Calcified Tissues and Biomaterials of the Université de Montréal, who holds a Canada Research Chair in Calcified Tissues, Biomaterials, and Structural Imaging, for his invaluable contribution * to the conceptualization of the project and to the high-resolution scanning electron microscopic analysis of the GDF-5-coated nanotopographic titanium surfaces (* Conceptualization, methodology, formal analysis/investigation, writing—review and editing, visualization and supervision).

Conflicts of Interest: The authors declare no conflicts of interest.

References

1. Lu, X.; Wang, Y.; Yang, X.; Zhang, Q.; Zhao, Z.; Weng, L.T.; Leng, Y. Spectroscopic analysis of titanium surface functional groups under various surface modification and their behaviors in vitro and in vivo. *J. Biomed. Mater. Res. A* **2008**, *84*, 523–534. [CrossRef] [PubMed]
2. Holmes, C.; Tabrizian, M. Surface Functionalization of Biomaterials. In *Stem Cell Biology and Tissue Engineering in Dental Sciences*; Vishwakarma, A., Sharpe, P., Shi, S., Ramalingam, M., Eds.; Academic Press: Cambridge, MA, USA, 2015; pp. 187–206. ISBN 9780123971579. [CrossRef]
3. Lumetti, S.; Manfredi, E.; Ferraris, S.; Spriano, S.; Passeri, G.; Ghiacci, G.; Macaluso, G.; Galli, C. The response of osteoblastic MC3T3-E1 cells to micro- and nano-textured, hydrophilic and bioactive titanium surfaces. *J. Mater. Sci. Mater. Med.* **2016**, *27*, 68. [CrossRef]
4. Trino, L.D.; Bronze-Uhle, E.S.; George, A.; Mathew, M.T.; Lisboa-Filho, P.N. Surface physicochemical and structural analysis of functionalized titanium dioxide films. *Colloids Surf. A Physicochem. Eng. Asp.* **2018**, *546*, 168–178. [CrossRef]
5. Harawaza, K.; Cousins, B.; Roach, P.; Fernandez, A. Modification of the surface nanotopography of implant devices: A translational perspective. *Mater. Today Bio* **2021**, *12*, 100152. [CrossRef]
6. Sánchez-Bodón, J.; Andrade Del Olmo, J.; Alonso, J.M.; Moreno-Benítez, I.; Vilas-Vilela, J.L.; Pérez-Álvarez, L. Bioactive Coatings on Titanium: A Review on Hydroxylation, Self-Assembled Monolayers (SAMs) and Surface Modification Strategies. *Polymers* **2021**, *14*, 165. [CrossRef]
7. Hou, C.; An, J.; Zhao, D.; Ma, X.; Zhang, W.; Zhao, W.; Wu, M.; Zhang, Z.; Yuan, F. Surface Modification Techniques to Produce Micro/Nano-scale Topographies on Ti-Based Implant Surfaces for Improved Osseointegration. *Front. Bioeng. Biotechnol.* **2022**, *10*, 835008. [CrossRef]
8. Li, J.; Zheng, Y.; Yu, Z.; Kankala, R.K.; Lin, Q.; Shi, J.; Chen, C.; Luo, K.; Chen, A.; Zhong, Q. Surface-modified titanium and titanium-based alloys for improved osteogenesis: A critical review. *Heliyon* **2023**, *10*, e23779. [CrossRef]
9. Davies, J.E. Understanding peri-implant endosseous healing. *J. Dent. Educ.* **2003**, *67*, 932–949. [CrossRef] [PubMed]
10. Subramani, K.; Jung, R.E.; Molenberg, A.; Hammerle, C.H. Biofilm on dental implants: A review of the literature. *Int. J. Oral Maxillofac. Implants.* **2009**, *24*, 616–626.
11. Ferraris, S.; Cochis, A.; Cazzola, M.; Tortello, M.; Scalia, A.; Spriano, S.; Rimondini, L. Cytocompatible and Anti-bacterial Adhesion Nanotextured Titanium Oxide Layer on Titanium Surfaces for Dental and Orthopedic Implants. *Front. Bioeng. Biotechnol.* **2019**, *7*, 103. [CrossRef]
12. Lopes, V.R.; Birgersson, U.; Manivel, V.A.; Hulsart-Billström, G.; Gallinetti, S.; Aparicio, C.; Hong, J. Human Whole Blood Interactions with Craniomaxillofacial Reconstruction Materials: Exploring In Vitro the Role of Blood Cascades and Leukocytes in Early Healing Events. *J. Funct. Biomater.* **2023**, *14*, 361. [CrossRef]
13. Hu, W.J.; Eaton, J.W.; Ugarova, T.P.; Tang, L. Molecular basis of biomaterial-mediated foreign body reactions. *Blood* **2001**, *98*, 1231–1238. [CrossRef]
14. Marucco, A.; Gazzano, E.; Ghigo, D.; Enrico, E.; Fenoglio, I. Fibrinogen enhances the inflammatory response of alveolar macrophages to TiO2, SiO2 and carbon nanomaterials. *Nanotoxicology* **2016**, *10*, 1–9. [CrossRef]
15. Wu, X.; Wang, C.; Hao, P.; He, F.; Yao, Z.; Zhang, X. Adsorption properties of albumin and fibrinogen on hydrophilic/hydrophobic TiO2 surfaces: A molecular dynamics study. *Colloids Surf. B Biointerfaces* **2021**, *207*, 111994. [CrossRef]
16. Petrie, T.A.; Reyes, C.D.; Burns, K.L.; García, A.J. Simple application of fibronectin-mimetic coating enhances osseointegration of titanium implants. *J. Cell Mol. Med.* **2009**, *13*, 2602–2612. [CrossRef]

17. Rapuano, B.E.; Lee, J.J.; MacDonald, D.E. Titanium alloy surface oxide modulates the conformation of adsorbed fibronectin to enhance its binding to α(5) β(1) integrins in osteoblasts. *Eur. J. Oral Sci.* **2012**, *120*, 185–194. [CrossRef]
18. Parisi, L.; Ghezzi, B.; Bianchi, M.G.; Toffoli, A.; Rossi, F.; Bussolati, O.; Macaluso, G.M. Titanium dental implants hydrophilicity promotes preferential serum fibronectin over albumin competitive adsorption modulating early cell response. *Mater. Sci. Eng. C Mater. Biol. Appl.* **2020**, *117*, 111307. [CrossRef]
19. Puleo, D.A.; Nanci, A. Understanding and controlling the bone-implant interface. *Biomaterials* **1999**, *20*, 2311–2321. [CrossRef]
20. Devescovi, V.; Leonardi, E.; Ciapetti, G.; Cenni, E. Growth factors in bone repair. *Chir. Org. Mov.* **2008**, *92*, 161–168. [CrossRef]
21. Bjelić, D.; Finšgar, M. The Role of Growth Factors in Bioactive Coatings. *Pharmaceutics* **2021**, *13*, 1083. [CrossRef] [PubMed]
22. Che, Z.; Sun, Q.; Zhao, Z.; Wu, Y.; Xing, H.; Song, K.; Chen, A.; Wang, B.; Cai, M. Growth factor-functionalized titanium implants for enhanced bone regeneration: A review. *Int. J. Biol. Macromol.* **2024**, *274 Pt 2*, 133153. [CrossRef]
23. Derynck, R.; Budi, E.H. Specificity, versatility, and control of TGF-β family signaling. *Sci. Signal.* **2019**, *12*, eaav5183. [CrossRef]
24. Urist, M.R.; DeLange, R.J.; Finerman, G.A. Bone cell differentiation and growth factors. *Science* **1983**, *220*, 680–686. [CrossRef]
25. Canalis, E. Effect of growth factors on bone cell replication and differentiation. *Clin. Orthop. Relat. Res.* **1985**, 246–263.
26. Lind, M.; Bünger, C. Factors stimulating bone formation. *Eur. Spine J.* **2001**, *10* (Suppl. S2), S102–S109. [CrossRef]
27. Shimono, K.; Oshima, M.; Arakawa, H.; Kimura, A.; Nawachi, K.; Kuboki, T. The effect of growth factors for bone augmentation to enable dental implant placement: A systematic review. *Jpn. Dent. Sci. Rev.* **2010**, *46*, 43–53. [CrossRef]
28. Storm, E.E.; Huynh, T.V.; Copeland, N.G.; Jenkins, N.A.; Kingsley, D.M.; Lee, S.J. Limb alterations in brachypodism mice due to mutations in a new member of the TGF beta-superfamily. *Nature* **1994**, *368*, 639–643. [CrossRef]
29. Francis-West, P.H.; Abdelfattah, A.; Chen, P.; Allen, C.; Parish, J.; Ladher, R.; Allen, S.; MacPherson, S.; Luyten, F.P.; Archer, C.W. Mechanisms of GDF-5 action during skeletal development. *Development* **1999**, *126*, 1305–1315. [CrossRef]
30. Kuniyasu, H.; Hirose, Y.; Ochi, M.; Yajima, A.; Sakaguchi, K.; Murata, M.; Pohl, J. Bone augmentation using rhGDF-5-collagen composite. *Clin. Oral Implants Res.* **2003**, *14*, 490–499. [CrossRef]
31. Yoshimoto, T.; Yamamoto, M.; Kadomatsu, H.; Sakoda, K.; Yonamine, Y.; Izumi, Y. Recombinant human growth/differentiation factor-5 (rhGDF-5) induced bone formation in murine calvariae. *J. Periodontal Res.* **2006**, *41*, 140–147. [CrossRef] [PubMed]
32. Nakamura, T.; Yamamoto, M.; Tamura, M.; Izumi, Y. Effects of growth/differentiation factor-5 on human periodontal ligament cells. *J. Periodontal Res.* **2003**, *38*, 597–605. [CrossRef]
33. Nickel, J.; Kotzsch, A.; Sebald, W.; Mueller, T.D. A single residue of GDF-5 defines binding specificity to BMP receptor I.B. *J. Mol. Biol.* **2005**, *349*, 933–947. [CrossRef]
34. Zhao, M.; Harris, S.E.; Horn, D.; Geng, Z.; Nishimura, R.; Mundy, G.R.; Chen, D. Bone morphogenetic protein receptor signaling is necessary for normal murine postnatal bone formation. *J. Cell Biol.* **2002**, *157*, 1049–1060. [CrossRef]
35. Li, H.; Li, Y.; Xiang, L.; Luo, S.; Zhang, Y.; Li, S. Therapeutic potential of GDF-5 for enhancing tendon regenerative healing. *Regen. Ther.* **2024**, *26*, 290–298. [CrossRef] [PubMed]
36. Guadarrama Bello, D.; Fouillen, A.; Badia, A.; Nanci, A. A nanoporous titanium surface promotes the maturation of focal adhesions and formation of filopodia with distinctive nanoscale protrusions by osteogenic cells. *Acta Biomater.* **2017**, *60*, 339–349. [CrossRef]
37. Kato, R.B.; Roy, B.; De Oliveira, F.S.; Ferraz, E.P.; De Oliveira, P.T.; Kemper, A.G.; Hassan, M.Q.; Rosa, A.L.; Beloti, M.M. Nanotopography directs mesenchymal stem cells to osteoblast lineage through regulation of microRNA-SMAD-BMP-2 circuit. *J. Cell Physiol.* **2014**, *229*, 1690–1696. [CrossRef]
38. Lopes, H.B.; Freitas, G.P.; Fantacini, D.M.C.; Picanço-Castro, V.; Covas, D.T.; Rosa, A.L.; Beloti, M.M. Titanium with nanotopography induces osteoblast differentiation through regulation of integrin αV. *J. Cell Biochem.* **2019**, *120*, 16723–16732. [CrossRef]
39. Abuna, R.P.F.; Oliveira, F.S.; Lopes, H.B.; Freitas, G.P.; Fernandes, R.R.; Rosa, A.L.; Beloti, M.M. The Wnt/β-catenin signaling pathway is regulated by titanium with nanotopography to induce osteoblast differentiation. *Colloids Surf. B Biointerfaces* **2019**, *184*, 110513. [CrossRef] [PubMed]
40. Vetrone, F.; Variola, F.; Tambasco de Oliveira, P.; Zalzal, S.F.; Yi, J.H.; Sam, J.; Bombonato-Prado, K.F.; Sarkissian, A.; Perepichka, D.F.; Wuest, J.D.; et al. Nanoscale oxidative patterning of metallic surfaces to modulate cell activity and fate. *Nano Lett.* **2009**, *9*, 659–665. [CrossRef]
41. Bueno, R.d.B.; Adachi, P.; Castro-Raucci, L.M.; Rosa, A.L.; Nanci, A.; Oliveira, P.T. Oxidative nanopatterning of titanium surfaces promotes production and extracellular accumulation of osteopontin. *Braz. Dent. J.* **2011**, *22*, 179–184. [CrossRef]
42. de Oliveira, P.T.; Zalzal, S.F.; Beloti, M.M.; Rosa, A.L.; Nanci, A. Enhancement of in vitro osteogenesis on titanium by chemically produced nanotopography. *J. Biomed. Mater. Res. A* **2007**, *80*, 554–564. [CrossRef] [PubMed]
43. Adamson, A.W.; Gast, A.P. The solid-liquid interface—Contact angle. In *Physical Chemistry of Surfaces*; Adamson, A.W., Gast, A.P., Eds.; John Wiley & Sons: New York, NY, USA, 1997; pp. 347–389.
44. Rajaraman, R.; Rounds, D.E.; Yen, S.P.; Rembaum, A. A scanning electron microscope study of cell adhesion and spreading in vitro. *Exp. Cell Res.* **1974**, *88*, 327–339. [CrossRef] [PubMed]

45. Mosmann, T. Rapid colorimetric assay for cellular growth and survival: Application to proliferation and cytotoxicity assays. *J. Immunol. Methods* **1983**, *65*, 55–63. [CrossRef]
46. Livak, K.J.; Schmittgen, T.D. Analysis of relative gene expression data using real-time quantitative PCR and the 2(-Delta Delta C(T)) Method. *Methods* **2001**, *25*, 402–408. [CrossRef] [PubMed]
47. Lowry, O.H.; Rosebrough, N.J.; Farr, A.L.; Randall, R.J. Protein measurement with the Folin phenol reagent. *J. Biol. Chem.* **1951**, *193*, 265–275. [CrossRef]
48. Gregory, C.A.; Gunn, W.G.; Peister, A.; Prockop, D.J. An Alizarin red-based assay of mineralization by adherent cells in culture: Comparison with cetylpyridinium chloride extraction. *Anal. Biochem.* **2004**, *329*, 77–84. [CrossRef] [PubMed]
49. Nikolidakis, D.; Meijer, G.J.; Oortgiesen, D.A.; Walboomers, X.F.; Jansen, J.A. The effect of a low dose of transforming growth factor beta1 (TGF-beta1) on the early bone-healing around oral implants inserted in trabecular bone. *Biomaterials* **2009**, *30*, 94–99. [CrossRef] [PubMed]
50. Kim, S.; Myung, W.C.; Lee, J.S.; Cha, J.K.; Jung, U.W.; Yang, H.C.; Lee, I.S.; Choi, S.H. The effect of fibronectin-coated implant on canine osseointegration. *J. Periodontal Implant. Sci.* **2011**, *41*, 242–247. [CrossRef] [PubMed]
51. Baranowski, A.; Klein, A.; Ritz, U.; Ackermann, A.; Anthonissen, J.; Kaufmann, K.B.; Brendel, C.; Götz, H.; Rommens, P.M.; Hofmann, A. Surface Functionalization of Orthopedic Titanium Implants with Bone Sialoprotein. *PLoS ONE* **2016**, *11*, e0153978. [CrossRef] [PubMed]
52. Wazen, R.M.; Kuroda, S.; Nishio, C.; Sellin, K.; Brunski, J.B.; Nanci, A. Gene expression profiling and histomorphometric analyses of the early bone healing response around nanotextured implants. *Nanomedicine* **2013**, *8*, 1385–1395. [CrossRef] [PubMed]
53. Medvedev, A.E.; Ng, H.P.; Lapovok, R.; Estrin, Y.; Lowe, T.C.; Anumalasetty, V.N. Effect of bulk microstructure of commercially pure titanium on surface characteristics and fatigue properties after surface modification by sand blasting and acid-etching. *J. Mech. Behav. Biomed. Mater.* **2016**, *57*, 55–68. [CrossRef]
54. Li, L.; Pan, Y.; Zhang, C.; Xing, Y.; Pu, C.; Shi, F.; Yang, Z.; Li, J.; Weng, J.; Xiao, D. Preparation of magnetic calcium phosphate microcarriers loaded with bisphosphate-modified GDF-5 for bottom-up bone tissue engineering. *Arab. J. Chem.* **2024**, *17*, 105638. [CrossRef]
55. Livingston, M.; Tan, A. Coating Techniques and Release Kinetics of Drug-Eluting Stents. *J. Med. Device* **2016**, *10*, 010801. [CrossRef] [PubMed]
56. James, A.W.; LaChaud, G.; Shen, J.; Asatrian, G.; Nguyen, V.; Zhang, X.; Ting, K.; Soo, C. A Review of the Clinical Side Effects of Bone Morphogenetic Protein-2. *Tissue Eng. Part B Rev.* **2016**, *22*, 284–297. [CrossRef]
57. Bungartz, M.; Kunisch, E.; Maenz, S.; Horbert, V.; Xin, L.; Gunnella, F.; Mika, J.; Borowski, J.; Bischoff, S.; Schubert, H.; et al. GDF5 significantly augments the bone formation induced by an injectable, PLGA fiber-reinforced, brushite-forming cement in a sheep defect model of lumbar osteopenia. *Spine J.* **2017**, *17*, 1685–1698. [CrossRef] [PubMed]
58. Sachse, A.; Hasenbein, I.; Hortschansky, P.; Schmuck, K.D.; Maenz, S.; Illerhaus, B.; Kuehmstedt, P.; Ramm, R.; Huber, R.; Kunisch, E.; et al. BMP-2 (and partially GDF-5) coating significantly accelerates and augments bone formation close to hydroxyapatite/tricalcium-phosphate/brushite implant cylinders for tibial bone defects in senile, osteopenic sheep. *J. Mater. Sci. Mater. Med.* **2023**, *34*, 31. [CrossRef] [PubMed]
59. Sullivan, A.M.; O'Keeffe, G.W. The role of growth/differentiation factor 5 (GDF5) in the induction and survival of midbrain dopaminergic neurones: Relevance to Parkinson's disease treatment. *J. Anat.* **2005**, *207*, 219–226. [CrossRef] [PubMed]
60. Tosatti, S.; Schwartz, Z.; Campbell, C.; Cochran, D.L.; VandeVondele, S.; Hubbell, J.A.; Denzer, A.; Simpson, J.; Wieland, M.; Lohmann, C.H.; et al. RGD-containing peptide GCRGYGRGDSPG reduces enhancement of osteoblast differentiation by poly(L-lysine)-graft-poly(ethylene glycol)-coated titanium surfaces. *J. Biomed. Mater. Res. A* **2004**, *68*, 458–472. [CrossRef] [PubMed]
61. Shimaoka, H.; Dohi, Y.; Ohgushi, H.; Ikeuchi, M.; Okamoto, M.; Kudo, A.; Kirita, T.; Yonemasu, K. Recombinant growth/differentiation factor-5 (GDF-5) stimulates osteogenic differentiation of marrow mesenchymal stem cells in porous hydroxyapatite ceramic. *J. Biomed. Mater. Res. A* **2004**, *68*, 168–176. [CrossRef]
62. Jin, L.; Li, X. Growth differentiation factor 5 regulation in bone regeneration. *Curr. Pharm. Des.* **2013**, *19*, 3364–3373. [CrossRef]
63. Kasten, P.; Beyen, I.; Bormann, D.; Luginbühl, R.; Plöger, F.; Richter, W. The effect of two point mutations in GDF-5 on ectopic bone formation in a beta-tricalciumphosphate scaffold. *Biomaterials* **2010**, *31*, 3878–3884. [CrossRef] [PubMed]
64. de Oliveira, P.T.; de Oliva, M.A.; Maximiano, W.M.; Sebastião, K.E.; Crippa, G.E.; Ciancaglini, P.; Beloti, M.M.; Nanci, A.; Rosa, A.L. Effects of a mixture of growth factors and proteins on the development of the osteogenic phenotype in human alveolar bone cell cultures. *J. Histochem. Cytochem.* **2008**, *56*, 629–638. [CrossRef] [PubMed]
65. Ohlebusch, B.; Borst, A.; Frankenbach, T.; Klopocki, E.; Jakob, F.; Liedtke, D.; Graser, S. Investigation of alpl expression and Tnap-activity in zebrafish implies conserved functions during skeletal and neuronal development. *Sci. Rep.* **2020**, *10*, 13321. [CrossRef]
66. Addison, W.N.; Masica, D.L.; Gray, J.J.; McKee, M.D. Phosphorylation-dependent inhibition of mineralization by osteopontin ASARM peptides is regulated by PHEX cleavage. *J. Bone Miner. Res.* **2010**, *25*, 695–705. [CrossRef]

67. Yadav, M.C.; Huesa, C.; Narisawa, S.; Hoylaerts, M.F.; Moreau, A.; Farquharson, C.; Millán, J.L. Ablation of osteopontin improves the skeletal phenotype of phospho1(−/−) mice. *J. Bone Miner. Res.* **2014**, *29*, 2369–2381. [CrossRef] [PubMed]
68. Chen, J.; Singh, K.; Mukherjee, B.B.; Sodek, J. Developmental expression of osteopontin (OPN) mRNA in rat tissues: Evidence for a role for OPN in bone formation and resorption. *Matrix* **1993**, *13*, 113–123. [CrossRef] [PubMed]
69. Hunter, G.K.; Goldberg, H.A. Nucleation of hydroxyapatite by bone sialoprotein. *Proc. Natl. Acad. Sci. USA* **1993**, *90*, 8562–8565. [CrossRef] [PubMed]
70. Midura, R.J.; Wang, A.; Lovitch, D.; Law, D.; Powell, K.; Gorski, J.P. Bone acidic glycoprotein-75 delineates the extracellular sites of future bone sialoprotein accumulation and apatite nucleation in osteoblastic cultures. *J. Biol. Chem.* **2004**, *279*, 25464–25473. [CrossRef] [PubMed]
71. Yang, Y.; Cui, Q.; Sahai, N. How does bone sialoprotein promote the nucleation of hydroxyapatite? A molecular dynamics study using model peptides of different conformations. *Langmuir* **2010**, *26*, 9848–9859. [CrossRef]